Supplementary Materials for

Tunable Phonon Polaritons in Atomically Thin van der Waals Crystals of Boron Nitride

S. Dai, Z. Fei, Q. Ma, A. S. Rodin, M. Wagner, A. S. McLeod, M. K. Liu, W. Gannett, W. Regan, K. Watanabe, T. Taniguchi, M. Thiemens, G. Dominguez, A. H. Castro Neto, A. Zettl, F. Keilmann, P. Jarillo-Herrero, M. M. Fogler, D. N. Basov*

*Corresponding author. E-mail: dbasov@physics.ucsd.edu

This PDF file includes:

Materials and Methods

Preparation and characterization of hBN crystals

Microcrystals of hBN were exfoliated from bulk samples and then transferred to Si wafers capped with 300 nm-thick SiO_2 layer. We explored bulk hBN samples from two different sources including commercially available samples (www.momentive.com) and also specimens synthesized by means of high pressure techniques as described in Ref. (*31*). We observed reproducible polaritonic effects irrespective of the origin of our microcrystals. Raman spectroscopy was applied to characterize the hBN crystals. (Fig. S1B). These Raman spectra were in accord with the literature data for high-quality hBN specimens (*32*). We note that one can easily distinguish hBN crystals of different thickness by their color under the optical microscope (Fig. S1A) (*33*).

Infrared nano-imaging and nano-FTIR

The nano-imaging and Fourier transform infrared nano-spectroscopy (nano-FTIR) data were obtained using a commercial scattering-type scanning near-field optical microscope (s-SNOM) (www.neaspec.com) based on a tapping-mode atomic force microscope (AFM). The tapping frequency and amplitude of the AFM are about 250 *kHz* and 70 nm, respectively. In Fig. S2, we show schematics of our infrared (IR) sources and of the s-SNOM system. These IR sources include tunable quantum cascade lasers (QCLs) (www.daylightsolutions.com) and a broad-band source based on a difference frequency generation (DFG) system (www.lasnix.com). In combination, these sources cover a broad frequency range from 700 to 2300 cm^{-1} (Fig. S2). By focusing the IR beam onto the metalized AFM tip, we were able to probe the polaritonic effects of hBN. The back-scattered signal by the tip is registered by pseudoheterodyne interferometric detection and then demodulated at the *n*-th harmonics of the tapping frequency yielding background free images. In this work, we chose *n* = 3 or 4.

Supplementary Text

Modeling near field spectra and images due to phonon polariton waves in hBN

1. Tip-launched surface waves

We start with describing a model that captures the essence of the observed real-space patterns in Figs. 1−3 on purely phenomenological grounds. This model assumes that the near-field contrast detected by the s-SNOM is in the linear response regime and is purely local. In other words, the deviation of the s-SNOM signal from the area average is given by some linear functional $E(\mathbf{r})$ of the electric potential $\phi(r)$ directly underneath the tip. The qualitative aspects of the results do not depend on the precise relation between $\phi(r)$ and $E(r)$ as long as this relation is linear. For definiteness, one can think that $E(\mathbf{r})$ represents the deviation of the *z*-component of the local electric field from its average value, so we use the term "field" to refer to it from now on. We

further assume that tip-launched polaritons are characterized by the radially symmetric field distribution ($r = |\boldsymbol{r}|$)

$$E(r) = E_0 e^{iqr} \times \begin{cases} e^{-r^2/4r_0^2}, & r < r_0 \\ e^{-1/4}(r_0/r)^{1/2}, & r \geq r_0 \end{cases}, \tag{S1}$$

where we take $r_0 = \lambda_p/4$ (the diffraction limit), λ_p is the phonon polariton wavelength. Eq. S1 is designed to have the property that $E(r)$ goes to a constant underneath the tip ($r \to 0$) and behaves as an outgoing cylindrical wave at large distances. The momentum of this wave is a complex number

$$q_p = q + i\kappa = q(1 + i\gamma) = \frac{2\pi}{\lambda_p}(1 + i\gamma), \tag{S2}$$

where $\gamma = \kappa/q$ is the loss factor defined in the main text.

2. Near-field images of phonon polaritons

The observed polariton interference fringes (Figs. 1−3) originate from the superposition of tip-launched polariton waves with those reflected back from the edges of the hBN crystals. The edge-reflected waves can be approximately calculated using the method of images. For a single edge (Fig. S3A), the total field under the tip (solid red arrow) is given by $E_{\text{tot}} = E(0) + E(2L)r_{sp}$, where L is the tip-edge distance, r_{sp} is the complex coefficient of reflection off the edge, and function $E(r)$ is given by Eq. S1.

For the tapered hBN crystal (Fig. 1), the polariton waves launched by the tip may experience multiple reflections. Therefore, we introduce the index $m = 1, 2, \ldots$ to label the waves that are reflected m times by the edges before arriving back to the tip; we refer to them as the m-th order waves. The locations of the corresponding image sources are obtained by m consecutive mirror reflections of the tip across the alternate edges. We refer to them as the m-th order images. In Fig. S3B we show these multiple tip images (hollow dots) for one representative tip position (solid green dot). We use the double index "m,n" to label the n-th ($n = 1$ or 2) possible position of the m-th order images. Let $d_{m,n}$ be the distance between the n-th position of the m-th order images and the tip. The total polaritonic field underneath the tip can be expressed as:

$$E_{\text{tot}} = \sum_m \sum_n E(d_{m,n})r_{sp}^m. \tag{S3}$$

Using this formula we computed E_{tot} for every position within a triangular area representing the tapered hBN crystal in Fig. 1 of the main text. For this particular sample geometry only $m \leq 3$ images contribute to the formation of the interference patterns in the field of view.

Our simulation results are shown in Fig. 1C of the main text. We find a good qualitative agreement with the actual data (Fig. 1B) using the parameters $\gamma = 0.055$ and $r_{sp} = -0.2 + 0.3i$, which are in accord with the phonon polariton line profiles (Fig. 3A). Simulation images for the different choices of γ value along with the experimental data are shown in Fig. S4. The fact that the absolute value of r_{sp} is smaller than unity suggests that either the reflection has a strong diffuse component or a significant amount of energy is dissipated into degrees of freedom other than the principal polariton branch ($l = 0$ in the main text). Among the dominant factors reducing the reflectivity of polaritons are the roughness as well as canted nature of the edges.

Besides analyzing the two-dimensional interference patterns, we also examined the line profiles (Fig. 3A). Noticing a marked resemblance between the observed phonon polariton

fringes and the plasmonic interference fringes in graphene (*20, 21*), we attempted to roughly estimate the former using the simulation developed previously for the latter. In this way, we again arrived at the estimated range $\gamma \approx 0.04-0.07$.

3. Optical constants and infrared reflectivity of hBN

The infrared reflectivity of boron nitride (BN) has been investigated by several groups (*26, 34-36*). A consensus is that both the in-plane and the out-of-plane dielectric function can each be described by a single Lorentzian:

$$\varepsilon_\mu = \varepsilon_{\infty\mu} + \varepsilon_{\infty\mu} \frac{(\omega_{LO,\mu})^2 - (\omega_{TO,\mu})^2}{(\omega_{TO,\mu})^2 - \omega^2 - i\omega\Gamma_\mu}, \quad \mu = \perp, //, \tag{S4}$$

with nearly the same values of the optical phonon frequencies $\omega_{TO,\mu}$ and $\omega_{LO,\mu}$ reported by all the groups. These values are also in a good agreement with the results of *ab initio* calculations (*37, 38*). However, we met some difficulty finding reliable experimental data in the literature for limiting high-frequency values $\varepsilon_{\infty\mu}$ and especially the optical phonon broadening Γ_μ. The aforementioned experiments studied boron nitride samples obtained by pyrolysis (*26*), chemical-vapor-deposition (CVD) (*34*), and magnetron sputtering (*35, 36*). All of these materials were composed of misoriented (angle spread $\theta \sim \pm 30^0$) grains of sub-10 nm size. For such small grain sizes, the linewidth broadening of the phonons can be considerably larger than what is expected in single-crystals, as was shown by Raman studies (*39, 40*). On the other hand, Γ_μ as small as a few cm^{-1} was estimated for the CVD-grown rhombohedral boron nitride. This material has the same in-plane layer structure and nearly the same phonon frequencies as CVD hBN but a much higher degree of crystallographic order (*34*). For all of the above reasons, in our calculations we used the parameters of Cai *et al.* (*37*) with the broadening $\Gamma_{//} = 4$ cm^{-1} and $\Gamma_\perp = 5$ cm^{-1} in order to reproduce the observed loss factor $\gamma \approx 0.055$ at 1550cm^{-1} (see Fig. 3F of the main text).

The dielectric function of Eq. S4 serves as input into the calculation of the complex reflectivity $r_p(q, \omega)$ and therefore of the phonon polariton dispersion. Although our system consisted of three layers: hBN, SiO$_2$, and Si, at large q relevant for our experiments, the electric field of the polaritons is mostly confined in the first two layers. Therefore, it is legitimate to approximate $r_p(q, \omega)$ by the reflectivity of a simpler hBN/SiO$_2$ structure. The $r_p(q, \omega)$ can be derived from the Fresnel equations for a three-layer structure shown in Fig. S5:

$$r_p = \frac{r_a + r_s e^{i2k_e^z d}}{1 + r_a r_s e^{i2k_e^z d}}, \tag{S5}$$

$$r_a = \frac{\varepsilon_\perp k_a^z - \varepsilon_a k_e^z}{\varepsilon_\perp k_a^z + \varepsilon_a k_e^z}$$

$$r_s = \frac{\varepsilon_s k_e^z - \varepsilon_\perp k_s^z}{\varepsilon_s k_e^z + \varepsilon_\perp k_s^z} \tag{S6}$$

where the subscripts "*a*", "$\perp$" and "*s*" refer to air, hBN (the component normal to the *c*-axis), and SiO$_2$, respectively. Functions r_a and r_s have the meaning of the reflectivity of the air/hBN and hBN/SiO$_2$ interfaces, d is the thickness of the hBN crystal and k_i^z represents the *z*-axis

momentum of the photon in layer i. For $i = a$ and s, it is given by $k_i^z = \sqrt{\varepsilon_i \frac{\omega^2}{c^2} - q^2}$ with ε_i being the dielectric function. The subscript "e" stands for "extraordinary ray" of hBN, which has uniaxial anisotropy. The corresponding momentum is $k_e^z = \sqrt{\varepsilon_\perp (\omega/c)^2 - \frac{\varepsilon_\perp}{\varepsilon_{//}} q^2}$ (41).

4. Derivation of Eq. 1 and the origin of the multiple polariton branches

At large q we can make the approximation $k_a^z \approx k_s^z \approx iq$ and

$$k_e^z = iq \frac{\sqrt{\varepsilon_\perp}}{\sqrt{\varepsilon_{//}}} = \frac{q}{\psi}, \tag{S7}$$

in the preceding formulas, which enables us to further simplify the expression for r_p. Using straightforward algebraic manipulations, one is led to the analytic solution for the poles of r_p, Eq. 1 of the main text. Alternatively, a more physical derivation can be offered as follows. If dissipation is neglected, so that both $\varepsilon_\perp$ and $\varepsilon_{//}$ are real, the admissible value of momentum k_e^z obey the Fabry-Perot quantization condition

$$2k_e^z d + 2\phi_a + 2\phi_s = 2\pi m, \tag{S8}$$

where $2\phi_a$ and $2\phi_s$ are the phases of the reflection coefficients r_a and $-r_s$, i.e.,. the phase shifts for (inner) reflection of the extraordinary ray at the hBN-air and hBN-substrate interfaces. From Eq. S5 and Eq. S6 we find

$$\phi_j = \arctan\left(\frac{\varepsilon_j}{\varepsilon_\perp \psi} \right), \quad j = a, s. \tag{S9}$$

Combining Eq. S7-S9 we arrive at

$$q = -\frac{\psi}{d}(-\pi m + \phi_a + \phi_s). \tag{S10}$$

It is convenient to define $l = -m = 0$, 1, … to ensure that Re $q > 0$. If the losses are now included, the in-plane momentum would acquire an imaginary part $q \to q + i\kappa$. After these substitutions Eq. S10 becomes the same as the desired result, Eq. 1.

According to Eq. 1, the $0 < \gamma < 1$ condition can be satisfied within the Reststrahlen bands of hBN confined within the transverse ω_{TO} and longitudinal ω_{LO} phonon frequencies (Fig. 3D). Our imaging data probe mainly the band due to the upper Reststrahlen band, from $\omega_{TO,\perp} = 1367$ cm^{-1} to $\omega_{LO,\perp} = 1610$ cm^{-1} (26) where $\varepsilon_\perp$ is real and negative, whereas $\varepsilon_{//}$ is almost real and positive. The polariton branches all start at $\omega_{TO,\perp}$ at low q and disperse with the positive slope ($\alpha = +$) towards the limiting value of $\omega_{LO,\perp} = 1610$ cm^{-1} at large q.

Instead of looking for the poles of r_p in the complex plane, one can determine the polariton dispersion from the maxima of Im r_p at real momenta. This numerical method gives results that closely agree with our analytical Eq. 1 at large q where the latter equation is valid, see Fig. 2E. The positions of high-intensity lines in this plot give q, while their apparent widths characterize the dissipation κ (10).

Let us now briefly discuss the multiple branches of the polariton dispersion. As explained above, the $l > 0$ branches have a simple interpretation as the Fabry-Perot resonances confined between the two interfaces of the hBN crystal. The same phenomenon occurs in planar waveguides, so these modes can be termed "waveguide modes" (*29*). In our case the polariton branches are separated from one another by equal increments $\frac{\pi\psi}{d}$ in the momentum space. It is unusual however that this number is real while q itself is much larger than the photon momentum. In other words, it is unusual to have propagating modes far outside the light-cone. This fact can be traced to parameter ψ (defined in Eq. 1 or Eq. S7) being real, which is unique to hyperbolic materials such as hBN. Unfortunately, none of the $l > 0$ modes has shown evident features in the experiments so far. Observation of these "waveguide" modes may have been inhibited by imperfections of the sample edges and the current signal/noise ratio limitation.

Finally, it may be worth commenting on applicability of our continuum-medium approach to hBN crystals with just a few atomic layers N. Experimentally, our Eq. 1 is seen to be in quantitative agreement with the measurements even in the thinnest samples reported here, $N = 3$. On the theory side, the answer can be gleaned from the theoretical calculations of Michel and Verberck (*42*). They suggest that a qualitatively new effect caused by decrease in the number of layers is the character of yet unobserved high-order polariton branches. These authors find that the total number of all branches is finite and equal to N in each Reststrahlen band. Thus, in monolayer hBN there should be only one and in bilayer only two polariton branches in each band. Since we do not see high-order branches even in thick crystals, this distinction cannot yet be verified.

5. Near field spectra simulation

The near-field scattering amplitude $s(\omega)$ shown in Fig. 2F (right) of the main text was computed using the expression for the reflectivity, which accounted for all possible layers (hBN, SiO_2, and Si). It has the same form as Eq. S4 except r_s is replaced by r_{sq}:

$$r_{sq} = \frac{r_s + r_q e^{i2k_s^z d_s}}{1 + r_s r_q e^{i2k_s^z d_s}}$$

$$r_q = \frac{\varepsilon_q k_s^z - \varepsilon_s k_q^z}{\varepsilon_q k_s^z + \varepsilon_s k_q^z} \quad , \tag{S11}$$

$$k_q^z = \sqrt{\varepsilon_q (\frac{\omega}{c})^2 - q^2}$$

where $d_s = 300$ nm is the SiO_2 thickness and $\varepsilon_q = 11.7$ is the IR dielectric constant of Si. The tip-sample interaction was treated within the quasi-static approximation in which the AFM tip was modeled as a perfectly conducting prolate spheroid of total length 600 nm and the curvature radius 30 nm, as described in our previous work (*28*). Figure 2F indicates that the modeling captures all the main features of the observed spectrum. Two features arise due to two effects. One is the behavior of the ordinary reflectivity r_p at nearly zero momentum, i.e., the photonic response of our hBN/SiO_2/Si system. The other ingredient is the $\omega-$ dependence of r_p at very large momenta $q \sim 10^5$ cm^{-1} set by the curvature radius of the tip and its typical distance from the sample, i.e., the polaritonic effect. The photonic response causes the deep minima at 820 cm^{-1}

and 1625 cm^{-1}. These minima occur near the longitudinal optical (LO) phonon frequencies of hBN, $\omega_{LO,//}$ and $\omega_{LO,\perp}$ at which the far-field reflectivity r_p is close to -1, see Eq. S11), so that the electric field at the surface, proportional to $1 + r_p$, vanishes. (Note that the far-field reflectivity is a very sharp function of frequency near $\omega_{LO,\perp}$. It rapidly changes from -1 to 0 as frequency increases, giving the well-known reflectivity minimum.) The far-field reflectivity is also responsible for the hump-dip structure near 1100 cm^{-1}, which comes from the optical phonon of the SiO$_2$ substrate. On the other hand, the resonances centered around 760 cm^{-1} and 1370 cm^{-1} are to a large extent due to the high *near-field* reflectivity, the raison d'être of the polaritons. The combination of the far- and near-field response functions anchors these peaks at the transverse optical (TO) frequencies.
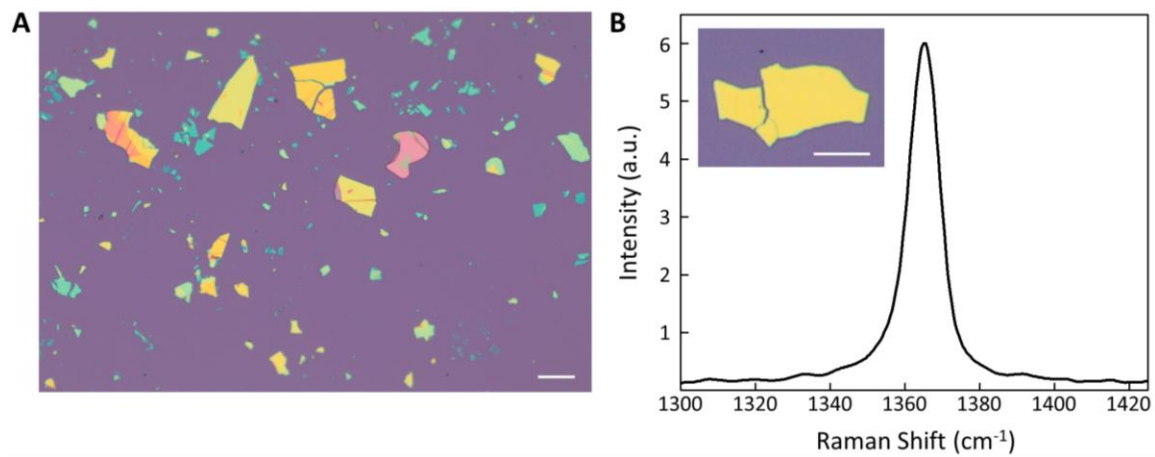
**Fig. S1. Optical microscope image and Raman spectrum of hBN.**
(**A**) hBN crystals of different thicknesses under the optical microscope. (**B**) Raman spectrum of the hBN crystal displayed in the inset. Scale bar: 30μm.
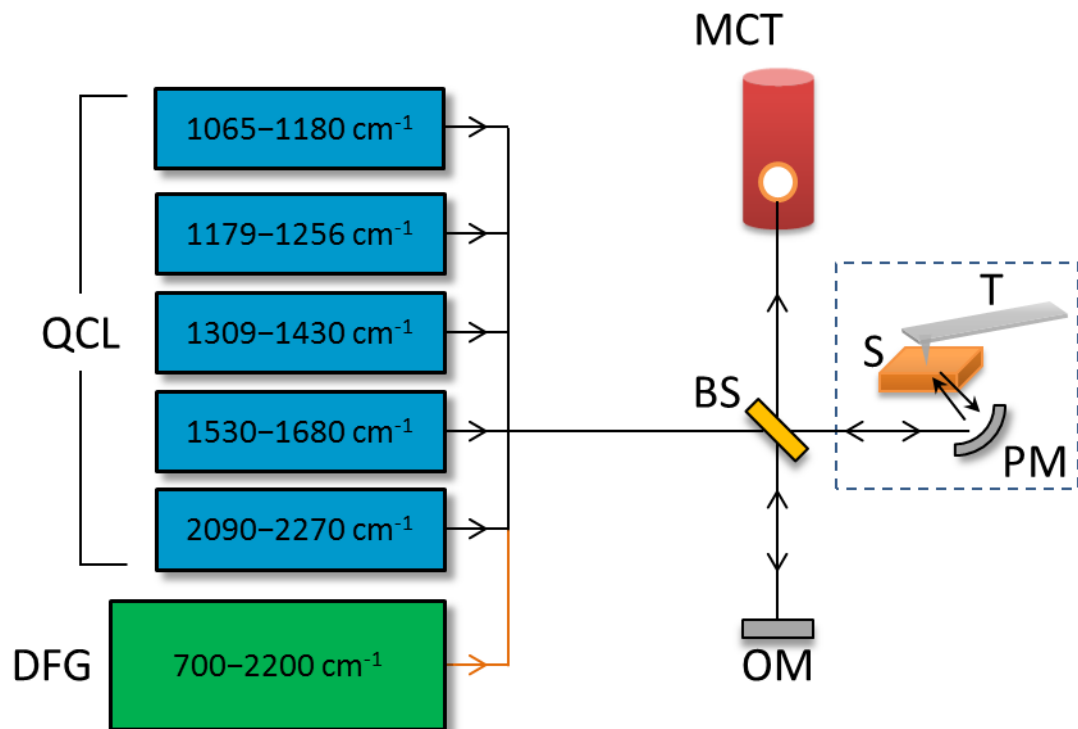
Fig. S2. Schematics of the UCSD s-SNOM for broad-band nano-imaging and nano-FTIR experiments.

Single frequency IR light (black arrows) is generated by 5 QCLs with tunable frequency indicated, in cm^{-1}. A broad-band beam (orange arrow) is generated by the DFG system with frequency range indicated. The IR beam enters an asymmetric interferometer composed of the elements: BS=ZnSe Beam Splitter, OM=Oscillating Mirror, MCT=Mercury Cadmium Telluride detector, PM=Parabolic Mirror, T=metallized Tip, S=Sample. Dashed box marks the s-SNOM part.
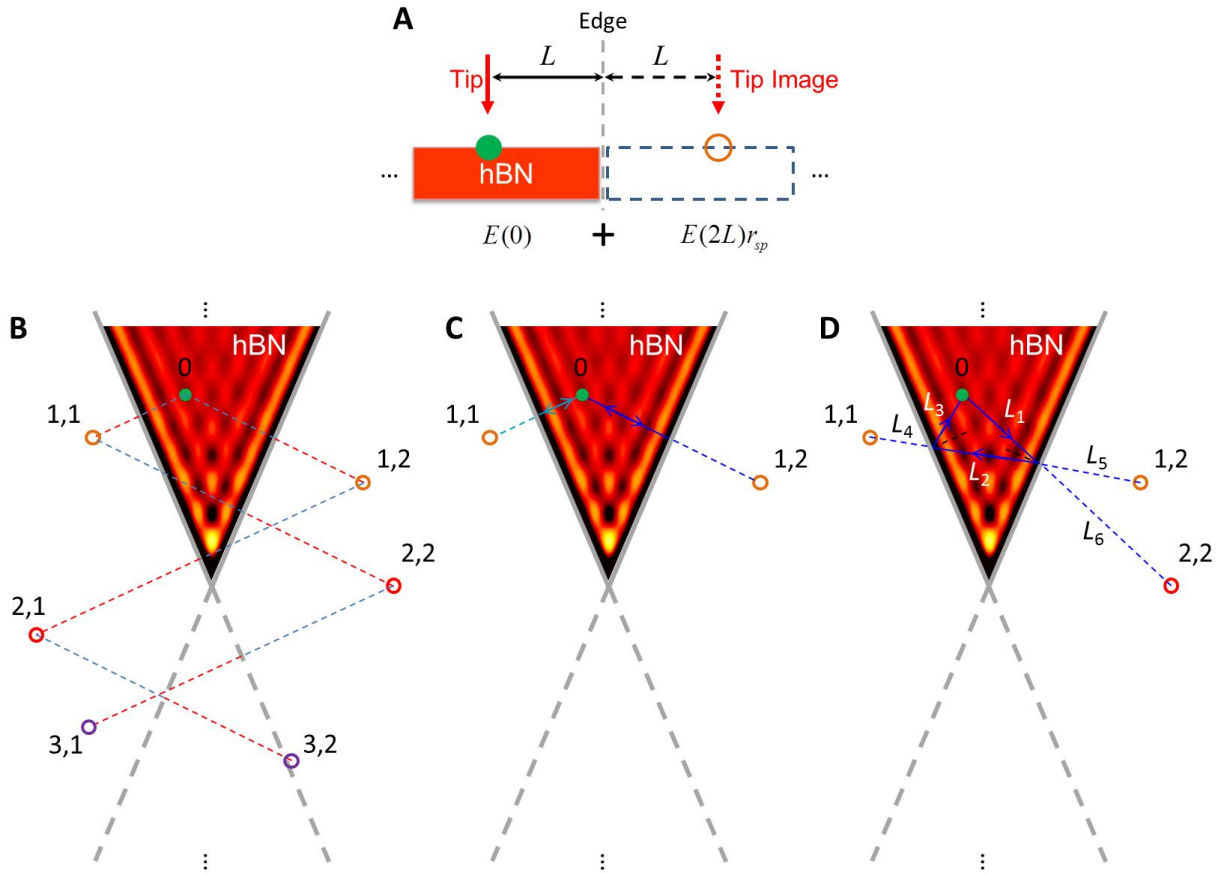
Fig. S3. Polaritonic waves in tapered crystals.
(**A**) Tip (solid red arrow) and its mirror image (dashed red arrow) according to the single hBN edge (grey dashed line). (**B**) A representative tip position (solid green dot, noted as "0") and its images (hollow dots, labeled as "*m,n*") for the simulation in Fig. 1C. Orange, red and purple dots mark the 1-st, 2-nd and 3-rd order images of the tip, respectively. Solid grey lines track the hBN crystal's edges; their extensions are shown with dashed lines. Red and blue dashed lines symmetrically connect the tip images with respect to the hBN edges. (**C**) The beam path (solid lines with arrow) of the 1-st order polariton waves. (**D**) The beam path (solid lines with arrow) of one representative 2-nd order polariton wave. L_1 to L_6 represent the length of each part in the solid (or dashed) blue line. Color map of (B-D): simulation results from Fig. 1C.
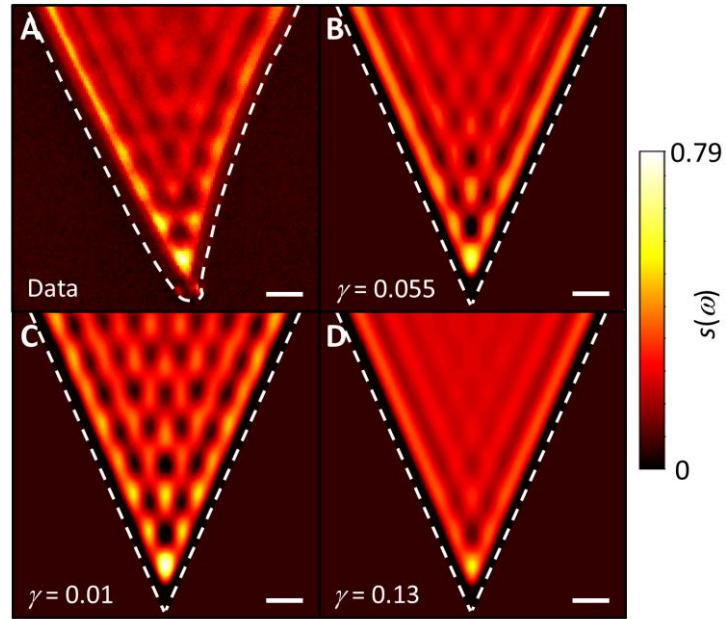
Fig. S4. Near-field image and simulation results with different loss factors.
(**A**) Near-field image of phonon polaritons from Fig. 1B of the main text. (**B**) Simulation image with the loss factor $\gamma = 0.055$ (Fig. 1C). (**C**) Simulation image with the loss factor $\gamma = 0.01$. (**D**) Simulation image with the loss factor $\gamma = 0.13$. Scale bar: 800 nm in all panels.
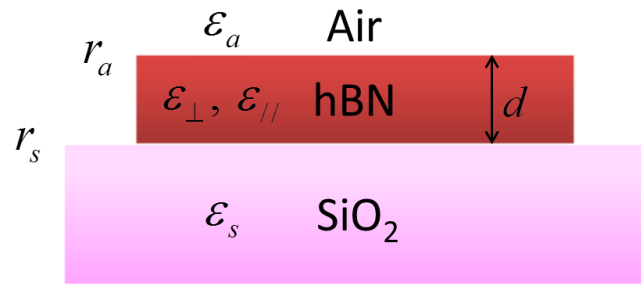
Fig. S5. Layered structure for the Air-hBN-SiO₂ system of the dispersion model.

References and Notes

1. C. R. Dean, A. F. Young, I. Meric, C. Lee, L. Wang, S. Sorgenfrei, K. Watanabe, T. Taniguchi, P. Kim, K. L. Shepard, J. Hone, Boron nitride substrates for high-quality graphene electronics. *Nat. Nanotechnol.* **5**, 722–726 (2010). Medline doi:10.1038/nnano.2010.172

2. K. S. Novoselov, D. Jiang, F. Schedin, T. J. Booth, V. V. Khotkevich, S. V. Morozov, A. K. Geim, Two-dimensional atomic crystals. *Proc. Natl. Acad. Sci. U.S.A.* **102**, 10451–10453 (2005). Medline doi:10.1073/pnas.0502848102

3. A. K. Geim, I. V. Grigorieva, Van der Waals heterostructures. *Nature* **499**, 419–425 (2013). Medline doi:10.1038/nature12385

4. T. Kimura, Y. Tokura, Layered magnetic manganites. *Annu. Rev. Mater. Sci.* **30**, 451–474 (2000). doi:10.1146/annurev.matsci.30.1.451

5. K. F. Mak, C. Lee, J. Hone, J. Shan, T. F. Heinz, Atomically thin MoS_2: A new direct-gap semiconductor. *Phys. Rev. Lett.* **105**, 136805 (2010). Medline doi:10.1103/PhysRevLett.105.136805

6. A. Splendiani, L. Sun, Y. Zhang, T. Li, J. Kim, C. Y. Chim, G. Galli, F. Wang, Emerging photoluminescence in monolayer MoS_2. *Nano Lett.* **10**, 1271–1275 (2010). Medline doi:10.1021/nl903868w

7. X. Qi, S. Zhang, Topological insulators and superconductors. *Rev. Mod. Phys.* **83**, 1057–1110 (2011). doi:10.1103/RevModPhys.83.1057

8. L. Britnell, R. M. Ribeiro, A. Eckmann, R. Jalil, B. D. Belle, A. Mishchenko, Y.-J. Kim, R. V. Gorbachev, T. Georgiou, S. V. Morozov, A. N. Grigorenko, A. K. Geim, C. Casiraghi, A. H. Castro Neto, K. S. Novoselov, Strong light-matter interactions in heterostructures of atomically thin films. *Science* **340**, 1311–1314 (2013); 10.1126/science.1235547. Medline doi:10.1126/science.1235547

9. S. Z. Butler, S. M. Hollen, L. Cao, Y. Cui, J. A. Gupta, H. R. Gutiérrez, T. F. Heinz, S. S. Hong, J. Huang, A. F. Ismach, E. Johnston-Halperin, M. Kuno, V. V. Plashnitsa, R. D. Robinson, R. S. Ruoff, S. Salahuddin, J. Shan, L. Shi, M. G. Spencer, M. Terrones, W. Windl, J. E. Goldberger, Progress, challenges, and opportunities in two-dimensional materials beyond graphene. *ACS Nano* **7**, 2898–2926 (2013). Medline doi:10.1021/nn400280c

10. L. Novotny, B. Hecht, *Principles of Nano-Optics* (Cambridge Univ. Press, Cambridge, 2006).

11. J. Renger, S. Grafström, L. M. Eng, R. Hillenbrand, Resonant light scattering by near-field-induced phonon polaritons. *Phys. Rev. B* **71**, 075410 (2005). doi:10.1103/PhysRevB.71.075410

12. S. Shen, A. Narayanaswamy, G. Chen, Surface phonon polaritons mediated energy transfer between nanoscale gaps. *Nano Lett.* **9**, 2909–2913 (2009). Medline doi:10.1021/nl901208v

13. T. Feurer, J. C. Vaughan, K. A. Nelson, Spatiotemporal coherent control of lattice vibrational waves. *Science* **299**, 374–377 (2003). [Medline](#) [doi:10.1126/science.1078726](#)

14. Y. De Wilde, F. Formanek, R. Carminati, B. Gralak, P. A. Lemoine, K. Joulain, J. P. Mulet, Y. Chen, J. J. Greffet, Thermal radiation scanning tunnelling microscopy. *Nature* **444**, 740–743 (2006). [Medline](#) [doi:10.1038/nature05265](#)

15. A. Huber, N. Ocelic, D. Kazantsev, R. Hillenbrand, Near-field imaging of mid-infrared surface phonon polariton propagation. *Appl. Phys. Lett.* **87**, 081103 (2005). [doi:10.1063/1.2032595](#)

16. T. Taubner, D. Korobkin, Y. Urzhumov, G. Shvets, R. Hillenbrand, Near-field microscopy through a SiC superlens. *Science* **313**, 1595 (2006). [Medline](#) [doi:10.1126/science.1131025](#)

17. G. Shvets, Photonic approach to making a material with a negative index of refraction. *Phys. Rev. B* **67**, 035109 (2003). [doi:10.1103/PhysRevB.67.035109](#)

18. J. A. Schuller, R. Zia, T. Taubner, M. L. Brongersma, Dielectric metamaterials based on electric and magnetic resonances of silicon carbide particles. *Phys. Rev. Lett.* **99**, 107401 (2007). [Medline](#) [doi:10.1103/PhysRevLett.99.107401](#)

19. Materials and methods are available as supplementary materials on *Science* Online.

20. J. Chen, M. Badioli, P. Alonso-González, S. Thongrattanasiri, F. Huth, J. Osmond, M. Spasenović, A. Centeno, A. Pesquera, P. Godignon, A. Z. Elorza, N. Camara, F. J. García de Abajo, R. Hillenbrand, F. H. Koppens, Optical nano-imaging of gate-tunable graphene plasmons. *Nature* **487**, 77–81 (2012). [Medline](#)

21. Z. Fei, A. S. Rodin, G. O. Andreev, W. Bao, A. S. McLeod, M. Wagner, L. M. Zhang, Z. Zhao, M. Thiemens, G. Dominguez, M. M. Fogler, A. H. Castro Neto, C. N. Lau, F. Keilmann, D. N. Basov, Gate-tuning of graphene plasmons revealed by infrared nano-imaging. *Nature* **487**, 82–85 (2012). [Medline](#)

22. F. Keilmann, S. Amarie, Mid-infrared frequency comb spanning an octave based on an Er fiber laser and difference-frequency generation. *J. Infrared Millimeter Terahertz Waves* **33**, 479–484 (2012). [doi:10.1007/s10762-012-9894-x](#)

23. J. M. Atkin, S. Berweger, A. C. Jones, M. B. Raschke, Nano-optical imaging and spectroscopy of order, phases, and domains in complex solids. *Adv. Phys.* **61**, 745–842 (2012). [doi:10.1080/00018732.2012.737982](#)

24. Z. Fei, G. O. Andreev, W. Bao, L. M. Zhang, A. S McLeod, C. Wang, M. K. Stewart, Z. Zhao, G. Dominguez, M. Thiemens, M. M. Fogler, M. J. Tauber, A. H. Castro-Neto, C. N. Lau, F. Keilmann, D. N. Basov, Infrared nanoscopy of dirac plasmons at the graphene-SiO_2 interface. *Nano Lett.* **11**, 4701–4705 (2011). [Medline](#) [doi:10.1021/nl202362d](#)

25. R. Hillenbrand, T. Taubner, F. Keilmann, Phonon-enhanced light matter interaction at the nanometre scale. *Nature* **418**, 159–162 (2002). [Medline](#) [doi:10.1038/nature00899](#)

26. R. Geick, C. H. Perry, G. Rupprecht, Normal modes in hexagonal boron nitride. *Phys. Rev.* **146**, 543–547 (1966). doi:10.1103/PhysRev.146.543

27. X. G. Xu, A. E. Tanur, G. C. Walker, Phase controlled homodyne infrared near-field microscopy and spectroscopy reveal inhomogeneity within and among individual boron nitride nanotubes. *J. Phys. Chem. A* **117**, 3348–3354 (2013). Medline [doi:10.1021/jp4008784](doi:10.1021/jp4008784)

28. L. M. Zhang, G. O. Andreev, Z. Fei, A. S. McLeod, G. Dominguez, M. Thiemens, A. H. Castro-Neto, D. N. Basov, M. M. Fogler, Near-field spectroscopy of silicon dioxide thin films. *Phys. Rev. B* **85**, 075419 (2012). doi:10.1103/PhysRevB.85.075419

29. A. Poddubny, I. Iorsh, P. Belov, Y. Kivshar, Hyperbolic metamaterials. *Nat. Photonics* **7**, 948–957 (2013). doi:10.1038/nphoton.2013.243

30. R. Stanley, Plasmonics in the mid-infrared. *Nat. Photonics* **6**, 409–411 (2012). doi:10.1038/nphoton.2012.161

31. K. Watanabe, T. Taniguchi, H. Kanda, Direct-bandgap properties and evidence for ultraviolet lasing of hexagonal boron nitride single crystal. *Nat. Mater.* **3**, 404–409 (2004). Medline doi:10.1038/nmat1134

32. R. V. Gorbachev, I. Riaz, R. R. Nair, R. Jalil, L. Britnell, B. D. Belle, E. W. Hill, K. S. Novoselov, K. Watanabe, T. Taniguchi, A. K. Geim, P. Blake, Hunting for monolayer boron nitride: Optical and Raman signatures. *Small* **7**, 465–468 (2011). Medline doi:10.1002/smll.201001628

33. D. Golla, K. Chattrakun, K. Watanabe, T. Taniguchi, B. J. LeRoy, A. Sandhu, Optical thickness determination of hexagonal boron nitride flakes. *Appl. Phys. Lett.* **102**, 161906 (2013). [doi:10.1063/1.4803041](doi:10.1063/1.4803041)

34. S. V. Ordin, B. N. Sharupin, M. I. Fedorov, Normal lattice vibrations and the crystal structure of anisotropic modifications of boron nitride. *Semiconductors* **32**, 924–932 (1998). [doi:10.1134/1.1187516](doi:10.1134/1.1187516)

35. E. Franke, M. Schubert, H. Neumann, T. E. Tiwald, D. W. Thompson, J. A. Woollam, J. Hahn, F. Richter, Phase and microstructure investigations of boron nitride thin films by spectroscopic ellipsometry in the visible and infrared spectral range. *J. Appl. Phys.* **82**, 2906 (1997). [doi:10.1063/1.366123](doi:10.1063/1.366123)

36. E. Franke, M. Schubert, J.-D. Hecht, H. Neumann, T. E. Tiwald, D. W. Thompson, H. Yao, J. A. Woollam, J. Hahn, *In situ* infrared and visible-light ellipsometric investigations of boron nitride thin films at elevated temperatures. *J. Appl. Phys.* **84**, 526 (1998). [doi:10.1063/1.368083](doi:10.1063/1.368083)

37. Y. Cai, L. Zhang, Q. Zeng, L. Cheng, Y. Xu, Infrared reflectance spectrum of BN calculated from first principles. *Solid State Commun.* **141**, 262–266 (2007). [doi:10.1016/j.ssc.2006.10.040](doi:10.1016/j.ssc.2006.10.040)

38. N. Ohba, K. Miwa, N. Nagasako, A. Fukumoto, First-principles study on structural, dielectric, and dynamical properties for three BN polytypes. *Phys. Rev. B* **63**, 115207 (2001). doi:10.1103/PhysRevB.63.115207

39. T. Kuzuba, K. Era, T. Ishii, T. Sato, A low frequency Raman-active vibration of hexagonal boron nitride. *Solid State Commun.* **25**, 863–865 (1978). doi:10.1016/0038-1098(78)90288-0

40. R. J. Nemanich, S. A. Solin, R. M. Martin, Light scattering study of boron nitride microcrystals. *Phys. Rev. B* **23**, 6348–6356 (1981). doi:10.1103/PhysRevB.23.6348

41. J. Lekner, Reflection ellipsometry of uniaxial crystals. *J. Opt. Soc. Am. A Opt. Image Sci. Vis.* **14**, 1359 (1997). doi:10.1364/JOSAA.14.001359

42. K. H. Michel, B. Verberck, Theoretical phonon dispersions in monolayers and multilayers of hexagonal boron-nitride. *Phys. Status Solidi B* **246**, 2802–2805 (2009). doi:10.1002/pssb.200982307